Title

Deep-learning-based cell composition analysis from tissue expression profiles.

Kevin Menden[$], Mohamed Marouf, Anupriya Dalmia, Peter Heutink, Stefan Bonn[$]

[$] Correspondence to sbonn@uke.de & Kevin.Menden@dzne.de

Abstract

We present Scaden, a deep neural network for cell deconvolution that uses gene expression information to infer the cellular composition of tissues. Scaden is trained on single cell RNA-seq data to engineer discriminative features that confer robustness to bias and noise, making complex data preprocessing and feature selection unnecessary. We demonstrate that Scaden outperforms existing deconvolution algorithms in both precision and robustness, across tissues and species. A single trained network reliably deconvolves bulk RNA-seq and microarray, human and mouse tissue expression data. Due to this stability and flexibility, we surmise that deep learning-based cell deconvolution will become a mainstay across data types and algorithmic approaches. Scaden's comprehensive software package is easy to use on novel as well as diverse existing expression datasets available in public resources, deepening the molecular and cellular understanding of developmental and disease processes.

Keywords

Cell Deconvolution, Deep Learning, Machine Learning, single cell RNA sequencing, RNA sequencing, Deep Sequencing, Source Separation.

Introduction

The analysis of tissue-specific gene expression using Next Generation Sequencing (RNA-seq) is a centerpiece of the molecular characterization of biological and medical processes[1]. A well-known limitation of tissue-based RNA-seq is that it typically measures average gene expression across many molecularly diverse cell types that can have distinct cellular states[2]. A change in gene expression between two conditions can therefore be attributed to a change in the cellular composition of the tissue or a change in gene expression in a specific cell population, or a mixture of the two. To deconvolve systematic differences in cell type composition is especially important in systems with cellular proliferation (e.g. cancer) or cellular death (e.g. neuronal loss in Neurodegenerative Diseases)[3].

To account for this problem, several computational cell deconvolution methods have been proposed during the last years[4,5]. These algorithms attempt to calculate an approximation of the cell type composition of a given gene expression sample, such that systematic differences in cellular abundance between samples can be detected, interpreted, and possibly corrected for. Current algorithms utilize gene expression profiles (GEPs) of cell type-specifically expressed genes to estimate cellular fractions using linear regression[4]. While the best performing linear regression algorithms for deconvolution seem to be variations of Support Vector Regression (SVR)[6–10], the selection of an optimal GEP is a field of active research[10,11]. Indeed, it has been recently shown that the design of the GEP is the most important factor in most deconvolution methods, as results from different algorithms strongly correlate given the same GEP[11].

In theory, an optimal GEP should contain a set of genes that are predominantly expressed within each cell population of a complex sample[12]. They should be stably

expressed across experimental conditions, for example across health and disease, and resilient to experimental noise and bias. The negative impact of bias on deconvolution performance can be partly improved by using large, heterogeneous GEP matrices[11]. It is therefore not surprising that recent advancement in cell deconvolution relied almost exclusively on sophisticated algorithms to normalize the data and engineer optimal GEPs[10].

While GEP-based approaches lay the foundational basis of modern cell deconvolution algorithms, we hypothesize that Deep Neural Networks (DNNs) could create optimal features for cell deconvolution, without relying on the complex generation of GEPs. DNNs such as multilayer perceptrons are universal function approximators that achieve state-of-the-art performance on classification and regression tasks. We theorize that by using gene expression information as network input, hidden layer nodes of the DNN would represent higher-order latent representations of cell types that are robust to input noise and technical bias.

An obvious limitation of DNNs is the requirement for large training data to avoid overfitting of the machine learning model. While ground truth information on tissue RNA-seq cell composition is scarce, one can use single cell RNA-seq (scRNA-seq) data to obtain virtually unlimited *in silico* tissue datasets of predefined cell composition[7–9,13–15]. This is achieved by sub-sampling and subsequently merging cells from scRNA-seq datasets and is limited only by the availability of tissue-specific scRNA-seq data. It is to be noted that scRNA-seq data suffers from known biases, such as drop-out, that RNA-seq data is not subject to[16]. While this complicates the use of scRNA-seq data for GEP design[8], we surmise that latent network nodes could represent features that are robust to such biases.

Based on these assumptions we developed a single-cell-assisted deconvolutional DNN (Scaden) that uses simulated bulk RNA-seq samples for training and predicts cell type proportions for input expression samples of cell mixtures. Scaden is trained on publicly available scRNA- and RNA-seq data, does not rely on specific GEP matrices, and automatically infers informative features. Finally, we show that Scaden deconvolves expression data into cell types with higher precision and robustness than existing methods that rely on GEP matrices, across tissues, species, and data types.

Results

Scaden Overview, Model Selection, and Training

The basic architecture of Scaden is a DNN that takes gene counts of RNA-seq data as input and outputs predicted cell fractions (Fig. 1). To optimize the performance of the DNN, it is trained on data that contains both the gene expression and the real cell fraction information (Fig. 1A). The network then adjusts its weights to minimize the error between the predicted cell fractions and the real cell fractions (Fig. 1B).

For the model selection and training we made use of the virtually unlimited amount of artificial bulk RNA-seq datasets with defined composition that can be generated *in silico* from published scRNA-seq and RNA-seq datasets (simulated tissues) (Fig. 1, Tables S1 & S2). The only constraint being that the scRNA-seq and RNA-seq data must come from the same tissue as the bulk data subject to deconvolution.

To find the optimal DNN architecture for cell deconvolution, we performed leave-one-dataset-out cross validation on simulated peripheral blood mononuclear cell (PBMC) tissue, training on mixtures of three scRNA-seq datasets and evaluating the performance on simulated tissue from a fourth scRNA-seq dataset (Table S1 & S3).

The final Scaden model is an ensemble of the three best performing models and the final cell type composition estimates are the averaged predictions of all three ensemble models (Fig. S1, Table S4).

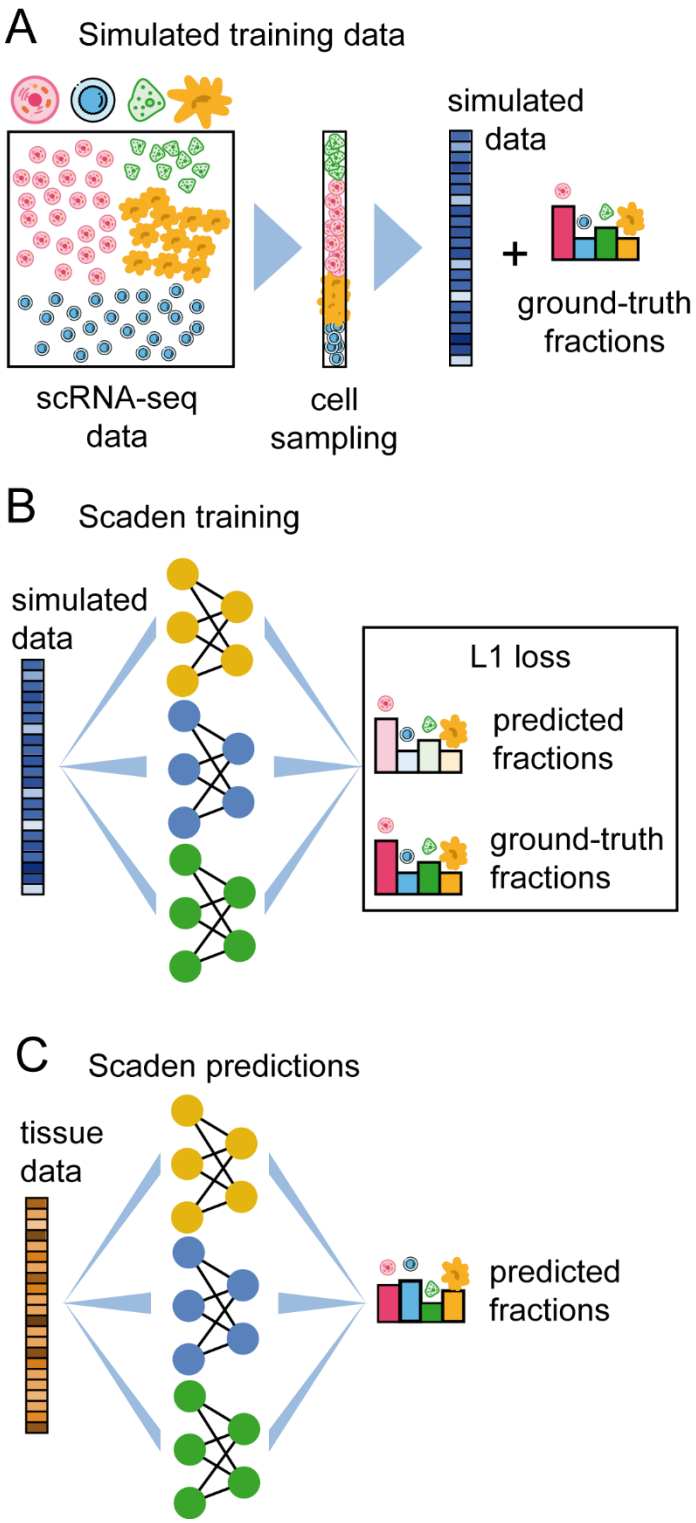

Figure 1 *Overview of training data generation and cell type deconvolution with Scaden*. A: Artificial bulk samples are generated by subsampling random cells from a scRNA-seq datasets and merging their expression profiles. B: Model training and parameter optimization on simulated tissue RNA-seq data by comparing cell fraction predictions to ground-truth cell composition. C: Cell deconvolution of real tissue RNA-seq data using Scaden.

To get an initial estimate of Scaden's deconvolution fidelity we measured the root mean square error (RMSE), Lin's concordance correlation coefficient (CCC)[17], Pearson's correlation coefficient (r), and the slope and intercept of the regression fitted for actual and predicted cell fractions. To this end, 32,000 human PBMC, 14,000 human pancreas, 6,000 human ascites, and 30,000 mouse brain simulated tissue datasets were generated for network training and evaluation (Table S2). We then compared Scaden to four state-of-the-art GEP-based cell deconvolution algorithms, CIBERSORT (CS)[6], CIBERSORTx (CSx)[7], MuSiC[8], and Cell Population Mapping (CPM)[9]. While CS relies on hand-curated GEP matrices, CSx, MuSiC, and CPM can generate GEPs using scRNA-seq data as input.

We first evaluated the deconvolution performance on simulated PBMC data, since curated GEP matrices and RNA-seq datasets with associated ground truth cell type compositions are available for human PBMCs, making this tissue uniquely suited toward deconvolution performance evaluation. Scaden was trained on simulated data from all datasets but a held-out dataset while CSx, MuSiC and CPM used a GEP generated from a scRNA-seq dataset excluding a held-out dataset (e.g. data6k, data8k, donorA). Subsequently the algorithms were tested on 500 simulated PBMC samples from a held-out scRNA-seq dataset (e.g. donorC) (Fig. 2A & B, Table S5). For CS we used the PBMC-optimized LM22 GEP matrix[6] and tested performance on the 500 simulated PBMC samples from a held-out scRNA-seq dataset (e.g. donorC).

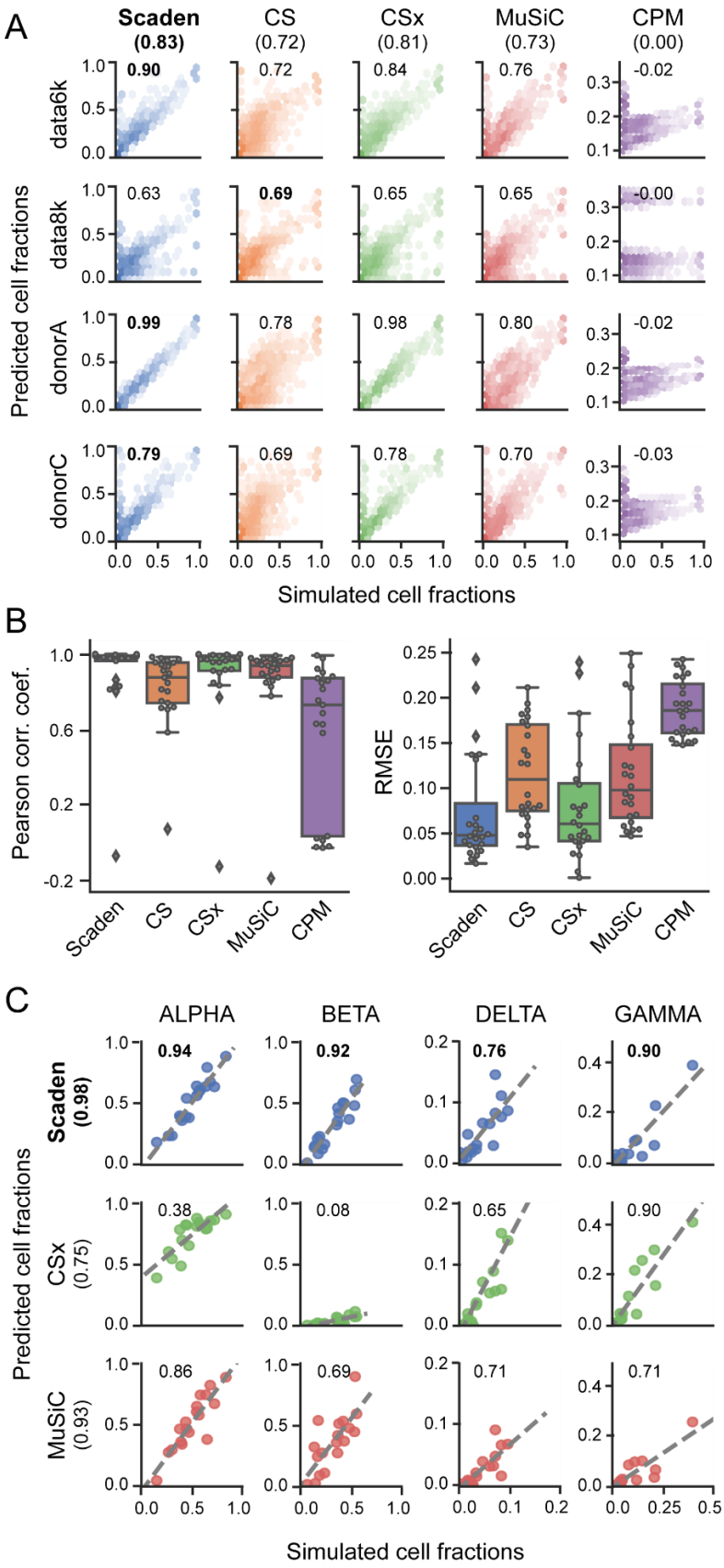

Figure 2 *Deconvolution performance on simulated tissue data* A: Ground truth values (x-axis) plotted against cell type fraction estimates (y-axis) for predictions made on simulated data

from four PBMC scRNA-seq datasets. Darker color in a hexbin corresponds to more data points falling into this bin. Numbers inside the plotting area signify CCC values, the overall CCC is shown in parenthesis below the algorithm name. B: Boxplots of r and RMSE values for simulated PBMC data. C: Per-cell-type scatterplots of ground truth (x-axis) and predicted values (y-axis) for Scaden, CSx, and MuSiC on artificial pancreas data[18]. Numbers inside the plotting area signify CCC values.

For three of four test datasets (data6k, donorA, donorC), Scaden obtained the highest CCC and lowest RMSE, followed by CSx, MuSiC, CS, and CPM (Fig. 2A, Table S5). For one test dataset, CS obtained the highest CCC and lowest RMSE, followed by CSx, MuSiC, Scaden and CPM. Overall, Scaden obtains the highest CCC and lowest RMSE (0.83, 0.09, respectively), followed by CSx (0.81, 0.10), MuSiC (0.73, 0.13), CS (0.72, 0.13), and CPM (0, 0.19) (Fig. 2A). As expected, all algorithms that use scRNA-seq data as reference perform good in this scenario with the notable exception of CPM, for which we could not generate reasonable predictions. We believe that CPM's modest performance might be due to the cell state mapping required by CPM. We created this mapping using UMAP, which might not be optimal for CPM. On average, Scaden also obtained the highest correlation and the best intercept and slope values on simulated PBMC data (Table S5).

A specific feature of the MuSiC algorithm is that it preferentially selects genes with low inter-subject and intra-cell cluster variability for its GEP, which increases deconvolution robustness when high expression heterogeneity is observed between human subjects, for example[8]. To understand if Scaden can utilize multi-subject information to increase its deconvolution performance, we trained Scaden, CSx, and MuSiC on scRNA-seq pancreas data from several subjects[19] and assessed the performance on a separate simulated pancreas RNA-seq dataset[18] (Fig. 2C, Table

S6). To allow for direct comparison, we chose the same pancreas training and test datasets that were used in the original MuSiC publication (Table S1). To enable Scaden to leverage the heterogeneity of multi-subject data, training data was generated separately for every subject in the dataset (see Methods). CSx cannot profit from multi-subject data, but performed well on the artificial PBMC datasets and was therefore included in the comparison. The best performance is achieved by Scaden (CCC = 0.98), closely followed by MuSiC (CCC = 0.93), while CSx does not perform as well (CCC = 0.75) (Fig. 2C, Table S6). This provides strong evidence that Scaden, by separating training data generation for each subject, can learn inter-subject heterogeneity and outperform specialized multi-subject algorithms such as MuSiC on the cell-type deconvolution task.

Robust deconvolution of bulk expression data

The true use case of cell deconvolution algorithms is the cell fraction estimation of tissue RNA-seq data. We therefore assessed the performance of Scaden, CS, CSx, MuSiC, and CPM to deconvolve two publicly available human PBMC bulk RNA-seq datasets, for which ground-truth cell composition information was measured using flow cytometry (Fig. 3A, Tables S7 & S8). We will refer to these datasets that consists of 12 samples each as PBMC1 [20] and PBMC2 [10]. Deconvolution for all methods was performed as described in the previous section, with the difference that data from all four PBMC scRNA-seq datasets was now deployed for Scaden training.

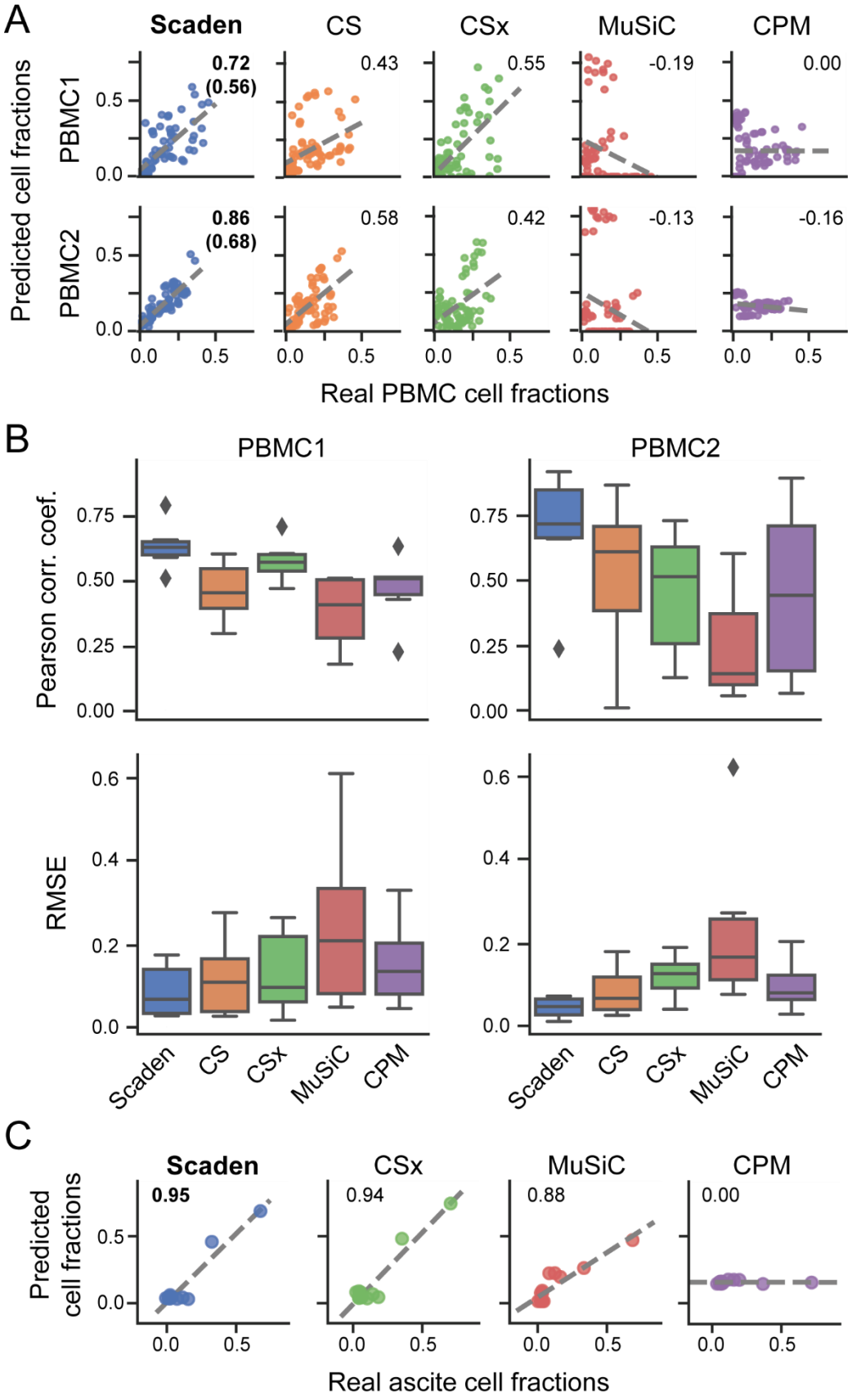

Figure 3 *Deconvolution of real tissue RNA-seq data* A: Per-cell-type scatterplots of ground truth (x-axis) and predicted values (y-axis) for Scaden, CS, CSx, MuSiC, and CPM on real

PBMC1 and PBMC2 cell fractions. Numbers inside the plotting area signify CCC values. For Scaden, the CCC using only scRNA-seq training data (in parenthesis) and the CCC using mixed scRNA-seq and RNA-seq training data is shown. B: Boxplots of r (first row) and RMSE (second row) values for real PBMC1 (first column) and PBMC2 (second column) data. C: Per-cell-type scatterplots of ground truth (x-axis) and predicted values (y-axis) for Scaden, CSx, MuSiC, and CPM on real ascite cell fractions. Numbers inside the plotting area signify CCC values.

On the PBMC1 dataset, Scaden obtained the highest CCC and lowest RMSE (0.56, 0.13), while CSx (0.55, 0.16) and CS (0.43, 0.15) performed well yet significantly worse than Scaden (Fig. 3A, Tables S8 & S9). CPM (0, 0.18) and MuSiC (-0.19, 0.32) both failed to deconvolve the cell fractions of the PBMC1 data. Scaden also obtained the best CCC and RMSE (0.68, 0.08) on the PBMC2 dataset, while CS (0.58, 0.10) and CSx (0.42, 0.13) obtained good deconvolution results. Similar to the PBMC1 data deconvolution results, CPM (-0.16, 0.11) as well as MuSiC (-0.13, 0.30) did not perform well on the PBMC2 deconvolution task. In addition to CCC and RMSE metrics, Scaden achieves the best correlation, intercept and slope on both PBMC datasets (Tables S8 & S9).

An additional algorithmic feature of Scaden is that it seamlessly integrates increasing amounts of training data, which can be of different types, such as a combination of simulated tissue and real tissue data with cell fraction information. In theory, even limited real tissue training data could make Scaden robust to data type bias and consequently improve Scaden's deconvolution performance on real tissue data. We therefore trained Scaden on a mix of simulated PBMC (500 samples) and real PBMC2 (12 samples) data and evaluated its performance on real PBMC1 data (Fig. 3A, S2, Table S9). While the training contained only ~2% real data, Scaden's CCC increased

from 0.56 to 0.72 and the RMSE decreased from 0.13 to 0.10. We observed similar performance increases when Scaden was trained on simulated PBMC and real PBMC1 data and evaluated on real PBMC2 data (Fig. 3A, S2, Table S9).

We next evaluated Scaden's performance real ascites RNA-seq data, for which scRNA-seq and FACS cell proportion data is available[21] (Table S7). It is noteworthy that RNA-seq, scRNA-seq, and FACS data was generated for the same samples, which potentially entails reduced experimental and technical bias and consequently higher deconvolution fidelity for the ascites data as compared to the PBMC data. We did not evaluate CS's performance on the ascites data as there was no optimized ascites GEP available. For Scaden, CSx, and MuSiC we used scRNA-seq data to generate simulated tissue ascites data for training. Scaden, CSx, CPM, and MuSiC all accurately predict the cell type compositions for the three real ascites samples, while CPM does not perform well (Fig. 3C, Table S10). The highest CCC and lowest RMSE were achieved by Scaden (0.95, 0.06), followed by CSx (0.94, 0.07), MuSiC (0.88, 0.08), and CPM (0, 0.18). This further validates that Scaden reliably deconvolves tissue RNA-seq data into the constituent cell fractions and that very accurate deconvolution results can be obtained if reference and target datasets are from the same experiment. Again, we surmise that CPM's drop in tissue RNA-seq deconvolution performance might be due to the required cell state space embedding, which makes deconvolution results not only depend on a good GEP matrix, but also on a good embedding. It might be that CPM's deconvolution suffers from the UMAP embedding used throughout this manuscript.

We next wanted to assess if Scaden's deconvolution performance is robust across species. We therefore tested whether a Scaden model trained on mouse brain scRNA-seq data could generate reasonable cell composition estimations for real human brain

RNA-seq data (Table S7). To this end, Scaden was trained on artificial data generated from five mouse brain scRNA-seq datasets and predicted the cell fractions on human post-mortem RNA-seq brain samples (390 prefrontal cortex samples) from the ROSMAP study[22]. Ground-truth cell fractions were not available for this data, which is why we used Braak stages[23] that correspond to Alzheimer's disease severity and correlate with the degree of neuronal loss. Overall, Scaden's cell fraction predictions capture the increased neuronal loss with increasing Braak stage (Fig. S3). Interestingly, the largest drop in neural percentage is observed at stage 5, when the neurodegeneration typically reaches the prefrontal cortex of the brain. By learning robust features, Scaden reliably deconvolves RNA-seq data in a cross-species comparison.

Given the robustness with which Scaden predicts tissue RNA-seq cell fractions using scRNA-seq training data, even across species, we next wanted to investigate if an scRNA-seq-trained Scaden model can also deconvolve other data types. To this end, we measured the deconvolution performance on a bulk PBMC microarray dataset (20 samples)[6] of a Scaden model trained on scRNA-seq and RNA-seq PBMC data (see above). We compared Scaden to CS using the microarray-derived LM22 matrix. CS achieved a slightly higher CCC and slightly lower total RMSE (0.72, 0.11) than Scaden (0.71, 0.13), while Scaden obtained the highest average CCC (0.50) compared to CS (0.39) (Fig. S4, Table S11). Notably in this scenario, Scaden was trained entirely on simulated data and RNA-seq data, while CS's LM22 GEP was optimized on PBMC microarray data.

Overall, we provide strong evidence that Scaden robustly deconvolves tissue data across tissues, species, and even data types.

Discussion

Scaden is the first deep learning-based cell deconvolution algorithm. In many instances, it compares favorably in both prediction robustness and accuracy to existing deconvolution algorithms that rely on GEP design and linear regression. We believe that Scaden's performance relies to a large degree on the inherent feature engineering of the DNN. The network does not only select features (genes) for regression, it also creates novel features that are optimal for the regression task in the nodes of the hidden layers. These hidden features are non-linear combinations of the input features (gene expression), which makes it notoriously difficult to explain how a DNN works[24]. It is important to highlight that this feature creation is fundamentally different from all other existing cell deconvolution algorithms, which rely on heuristics that select a defined subset of genes as features for linear regression.

Another advantage of this inherent feature engineering is that Scaden can be trained to be robust to input noise and bias (e.g. batch effects). Noise and bias is all prevalent in experimental data, due to different sample quality, sample processing, experimenters, and instrumentation, for example. If the network is trained on different datasets of the same tissue, however, it learns to create hidden features that are robust to noise and bias, such as batch effects. This robustness is pivotal in real world cell deconvolution use cases, where the bulk RNA data for deconvolution and the training data (and therefore the network and GEP) contain different noise and biases. While especially recent cell deconvolution algorithms include batch correction heuristics prior to GEP construction, Scaden optimizes its hidden features automatically when trained on data from various batches.

The robustness to noise and bias, which might be due to hidden feature generation, is especially evident in Scaden's ability to deconvolve across data types. A network

trained on *in silico* bulk RNA-seq data can seamlessly deconvolve microarray data of the same tissue. This is quite noteworthy, as microarray data is known to have a reduced dynamic range and several hybridization-based biases compared to RNA-seq data. In other words, Scaden can deconvolve bulk data of types it has never been trained on, even in the face of strong data type bias. This raises the possibility that Scaden trained on scRNA-seq data might reliably deconvolve other bulk omics data as well, such as proteomic and metabolomic data. This assumption is strengthened by the fact that Scaden, trained on scRNA-seq data, attains state-of-the-art performance on the deconvolution of bulk RNA-seq data, two data types with very distinct biases[16].

As highlighted in the introduction, a drawback for many DNNs is the large amount of training data required to obtain robust performance. Here, we used scRNA-seq data to create virtually unlimited amounts of *in silico* bulk RNA-seq data of predefined type (target tissue) with known composition, across datasets. This immediately highlights Scaden's biggest limitation, the dependency on scRNA-seq data of the target tissue. In this study we have shown that Scaden, trained solely on simulated data from scRNA-seq datasets, can outperform GEP-based deconvolution algorithms. We did observe, however, that the addition of labeled RNA-seq samples to the training data did significantly improve deconvolution performance in the case of PBMC data. We therefore believe that efforts to increase the similarity between simulated training data and the target bulk RNA-seq data could increase Scaden's performance further. Mixtures of *in silico* bulk RNA-seq data and publically available RNA-seq data, of purified cell types for example, could further increase the deconvolution performance of Scaden. Furthermore, domain adaptation methods can be used to improve performance of models that are trained on data (here, scRNA-seq data) that is similar

303 to the target data (here, RNA-seq data)[25]. In future versions, Scaden's simple
304 multilayer perceptron architecture could leverage domain adaptation to further
305 stabilize and improve its cell deconvolution performance.
306 Recent cell deconvolution algorithms have used cell fraction estimates to infer cell
307 type-specific gene expression from bulk RNA-seq data. It is straightforward to use
308 Scaden's cell fraction estimates to infer per group[3] and per sample[7] cell type-specific
309 gene expression using simple regression or non-negative matrix factorization,
310 respectively. We would like to add a note of caution, however, as the error of cell
311 fraction estimates, which can be quite significant, is propagated into the gene
312 expression calculations and will affect any downstream statistical analysis.
313 In summary, the deconvolution performance, robustness to noise and bias, the
314 flexibility to learn from large numbers of *in silico* datasets, across data types (scRNA-
315 seq and RNA-seq mixtures), and potentially even tissues makes us believe that DNN-
316 based architectures will become an algorithmic mainstay of cell type deconvolution.
317

Methods

Datasets and pre-processing

scRNA-seq datasets

The following human PBMC scRNA-seq datasets were downloaded from the 10X Genomics data download page: 6k PBMCs from a Healthy Donor, 8k PBMCs from a Healthy Donor, Frozen PBMCs (Donor A), Frozen PBMCs (Donor C){Zheng et al, 2017}. Throughout this paper, these datasets are referred to with the handles data6k, data8k, donorA and donorC, respectively. These four datasets were chosen because of clearly identifiable cell types for the majority of cells. The Ascites scRNA-seq dataset was downloaded from https://figshare.com as provided by Schelker[21]**.** Pancreas and mouse brain datasets were downloaded from the scRNA-seq dataset collection of the Hemberg lab (https://hemberg-lab.github.io/scRNA.seq.datasets/). A table listing all datasets including references to the original publications can be found in Table S1.

scRNA-seq preprocessing and analysis

All datasets were processed using the Python package Scanpy (v. 1.2.2)[26] following the Scanpy's reimplementation of the popular Seurat's clustering workflow. First, the corresponding cell-gene matrices were filtered for cells with less than 500 detected genes, and genes expressed in less than 5 cells. The resulting count matrix for each dataset was filtered for outliers with high or low numbers of counts. Gene expression was normalized to library size using the Scanpy function 'normalize_per_cell'. The normalized matrix of all filtered cells and genes was saved for the subsequent data generation step.

The following processing and analysis steps had the sole purpose of assigning cell type labels to every cell. All cells were clustered using the louvain clustering implementation of the Scanpy package. The louvain clustering resolution was chosen for each dataset, using the lowest possible resolution value (low resolution values lead to less clusters) for which the calculated clusters separated the cell types appropriately. The top 1000 highly variable genes were used for clustering, which were calculated using Scanpy's 'filter_genes_dispersion' function with parameters min_mean=0.0125, max_mean=3 and min_disp=0.5. Principal Component Analysis (PCA) was used for dimensionality reduction.

To identify cell types, marker genes were investigated for all cell types in question. For PBMC datasets, useful marker genes were adopted from public resources such as the Seurat tutorial for 2700 PBMCs[27]. Briefly, IL7R was taken as marker for CD4 T-cells, LYZ for Monocytes, MS4A1 for B-cells, GNLY for Natural Killer cells, FCER1A for Dendritic cells and CD8A and CCL5 as markers for CD8 T-cells. For all other scRNA-seq datasets, marker genes and expected cell types were inferred from the original publication of the dataset. For instance, to annotate cell types of the mouse brain dataset from Zeisel et al.[28], we used the same marker genes as Zeisel and colleagues. We did not use the same cell type labels from the original publications because a main objective was to assure that cell type labeling is consistent between all datasets of a certain tissue.

Cell type annotation was performed manually across all the clusters for each dataset, such that all cells belonging to the same cluster were labeled with the same cell type. The cell type identity of each cluster was chosen by crossing the cluster's highly differentially expressed genes with the curated cell type's marker genes. Clusters that

could not be clearly identified with a cell type were grouped into the 'Unknown' category.

Tissue Datasets for Benchmarking

To assess the deconvolution performance on real tissue expression data, we used datasets for which the corresponding cell fractions were measured and published. The first dataset is the **PBMC1** dataset which was obtained from Zimmermann *et al.*[20]. The second dataset, **PBMC2**, was downloaded from GEO with accession code GSE107011 [10]. This dataset contains both RNA-seq profiles of immune cells (S4 cohort) and from bulk individuals (S13 cohort). As we were interested in the bulk profiles, we only used 12 samples from the S13 cohort from this data. Flow cytometry fractions were collected from the Monaco *et al.* publication[10].

In addition to the above mentioned two PBMC datasets, we used Ascites RNA-seq data. This dataset was kindly provided by the authors and cell type fractions for this dataset were taken from the supplementary materials of the publication[21].

For the evaluation on pancreas data, artificial bulk RNA-seq samples created from the scRNA-seq dataset of Xin *et al*.[18] were used. This dataset was downloaded from the resources of the MuSiC publication[8]. The artificial bulk RNA-seq samples used for evaluation were then created using the 'bulk_construct' function of the MuSiC tool.

To assess how Scaden deals with unknown cell types in a bulk mixture, we used the whole blood dataset from Newman *et al*.[7], which consists of 12 samples (GSE127813). Cell type fractions were downloaded from the CSx website (https://cibersortx.stanford.edu/download.php).

The microarray dataset GSE65133 was downloaded from GEO, and cell type fractions taken from the original CS publication[6].

Finally, we wanted to get insights into neurodegenerative cell fraction changes in the brain. While it is known that neurodegenerative diseases like Alzheimer's Disease are accompanied by a gradual loss of brain neurons, stage-specific cell type shifts are still hard to come by. Here we use the ROSMAP (Religious Orders Study and Memory and Aging Project Study) cortical RNA-seq dataset along with the corresponding clinical metadata, to infer cell type composition over six clinically relevant stages of neurodegeneration[22].

RNA-seq preprocessing and analysis

For the RNA-seq datasets analyzed in this study, we did not apply any additional processing steps, but used the obtained count or expression tables directly as downloaded for all dataset except the ROSMAP dataset. For the latter, we generated count tables from raw FastQ-files using Salmon[29] and the GRCh38 reference genome. FastQ-files from the ROSMAP study were downloaded from Synapse (www.synapse.org).

Simulation of bulk RNA-seq samples from scRNA-seq data

Scadan's deep neural network requires large amounts of training RNA-seq samples with known cell fractions. This explains why the generation of artificial bulk RNA-seq data is one of the key elements of the Scaden workflow.

In order to generate the training data, preprocessed scRNA-seq datasets were used (see section 'Data Collection and Processing'), comprising the gene expression matrix and the cell type labels. Artificial RNA-seq samples were simulated by sub-sampling cells from individual scRNA-seq datasets - cells from different datasets were not merged into samples to preserve within-subject relationships. Datasets generated from multiple subjects were split according to subject and each sub-sampling was

412 constrained to cells from one subject in order to capture the cross-subject
413 heterogeneity and keep subject-specific gene dependencies.
414 The exact sub-sampling procedure is described in the following. First, for every
415 simulated sample, random fractions were created for all different cell types within each
416 scRNA-seq dataset using the random module of the Python package NumPy. Briefly,
417 a random number was chosen from a uniform distribution between 0 and 1 using the
418 NumPy function 'random.rand()' for each cell type, and then this number was divided
419 by the sum of all random numbers created to ensure the constraint of all fractions
420 adding up to 1:

421 $$f_c = \frac{r_c}{\sum_{C_{all}} r_c}$$

422 where $r_c$is the random number created for cell type c, and C_{all} is the set of all cell
423 types. Here, f_c is the calculated random fraction for cell type c. Then, each fraction
424 was multiplied with the total number of cells selected for each sample, yielding the
425 number of cells to choose for a specific cell type:
426
427 $$N_c = f_c * N_{total}$$
428
429 where N_c is the number of cells to select for the cell type c, and N_{total} is the total
430 number of cells contributing to one simulated RNA-seq sample (400, in this study).
431 Next, N_c cells were randomly sampled from the scRNA-seq gene expression matrix
432 for each cell type c. Afterwards, the randomly selected single-cell expression profiles
433 for every cell type are then aggregated by summing their expression values, to yield
434 the artificial bulk expression profile for this sample.
435 Using the above described approach, cell compositions that are strongly biased
436 toward a certain cell type or are missing specific cell types are rare among the
437 generated training samples. To account for this and to simulate cell compositions with

a heavy bias to and the absence of certain cell types, a variation of the sub-sampling procedure was used to generate samples with sparse compositions, which we refer to as sparse samples. Before generating the random fractions for all cell types, a random number of cell types was selected to be absent from the sample, with the requirement of at least one cell type constituting the sample. After these leave-out cell types were chosen, random fractions were created and samples generated as described above. Using this procedure, we generated 32,000 samples for the human PBMC training dataset, 14,000 samples for the human pancreas training dataset and 30,000 samples for the mouse brain training dataset (Table S2).

Artificial bulk RNA-seq datasets were stored in 'h5ad' format using the Anndata package[26], which allows to store the samples together with their corresponding cell type ratios, while also keeping information about the scRNA-seq dataset of origin for each sample. This allowed to access samples from specific datasets, which is useful for cross validation.

Scaden Overview

The following section contains an overview of the input data preprocessing, the Scaden model, model selection, and how Scaden predictions are generated.

Input Data Preprocessing

The data preprocessing step is aimed to make the input data more suitable for machine learning algorithms. To achieve this, an optimal preprocessing procedure should transform any input data from the simulated samples or from the bulk RNA-seq to the same feature scale. Before any scaling procedure can be applied, it must be ensured that both the training data and the bulk RNA-seq data subject to prediction share the same features. Therefore, before scaling, both datasets are limited to

462 contain features (genes) that are available in both datasets.. The two-step processing
463 procedure used for Scaden is described in the following:
464 First, to account for heteroscedasticity, a feature inherent to RNA-seq data, the data
465 was transformed into logarithmic space by adding a pseudocount of 1 and then taking
466 the Logarithm (base 2). Additional to stabilizing the variance, this transformation yields
467 data that is approximately Gaussian.
468 Second, every sample was scaled to the range [0,1] using the MinMaxScaler() class
469 from the Sklearn preprocessing module {ref}. Per sample scaling, unlike per feature
470 scaling that is more common in machine learning, assures that inter-gene relative
471 expression patterns in every sample are preserved. This is important, as our
472 hypothesis was that a neural network could learn the deconvolution from these inter-
473 gene expression patterns.

474 $$x_{scaled,i} = (x_i - min(\boldsymbol{X}_i)) \,/\, (max(X_i) - min(X_i))$$

475 where $x_{scaled,i}$ is the log2 expression value of gene x in sample i, X_i is the vector of
476 log2 expression values for all genes of sample i, $min(\boldsymbol{X}_i)$ is the minimum gene
477 expression of vector X_i, and $max(X_i)$ the maximum gene expression of vector X_i.
478 Note that all training datasets are stored as expression values and are only processed
479 as described above. In the deployment use-case the simulated training data should
480 contain the same features as in the bulk RNA-seq sample that shall be deconvolved.

481 ## Model Selection

482 The goal of model selection was to find an architecture and hyperparameters that
483 robustly deconvolve simulated tissue RNA-seq data and, more importantly, real bulk
484 RNA-seq data. Due to the very limited availability of bulk RNA-seq datasets with known
485 cell fractions, model selection was mainly optimized on the simulated PBMC datasets.

To capture inter-experimental variation, we used leave-one-dataset-out cross validation for model optimization: a model was trained on simulated data from all but one dataset, and performance was tested on simulated samples from the left-out dataset. This allows to simulate batch effects between datasets and helps to test the generalizability of the model. Model performance was evaluated based on pearson product moment correlation and absolute deviation between predicted and ground truth values. As averaging the predictions of models with different architectures increased performance, we decided to use an ensemble architecture for Scaden. For this ensemble, the three best performing architectures were chosen. Model training and prediction is done separately for each model, with the prediction averaging step combining all model predictions (Fig. S1). We provide a list of all tested parameters in the supplementary materials (Table S4).

Final Scaden Model

The Scaden model learns cell type deconvolution through supervised training on datasets of simulated bulk RNA-seq samples simulated with scRNA-seq data. To account for model biases and to improve performance, Scaden consists of an ensemble of three deep neural networks with varying architectures and degrees of dropout regularization. All models of the ensemble use four layers of varying sizes between 32 and 1024 nodes, with dropout-regularization implemented in two of the three ensemble models. The exact layer sizes and dropout rates are listed in Table S3. The Rectified Linear Unit (ReLU) is used as activation function in every internal layer. We used a Softmax function to predict cell fractions, as we did not see any improvements in using a linear output function with consecutive non-negativity correction and sum-to-one scaling. Python (v. 3.6.6) and the TensorFlow library (v.

1.10.0) were used for implementation of Scaden. A complete list of all software used for the implementation of Scaden is provided in Table S12.

Training and Prediction

After the preprocessing of the data a Scaden ensemble can be trained on simulated tissue RNA-seq data or mixtures of simulated and real tissue RNA-seq data. Parameters are optimized using Adam with a learning rate of 0.0001 and a batch size of 128. We used an L1 loss as optimization objective:

$$L1(y_i, \hat{y}_i) = |y_i - \hat{y}_i|$$

where y_i is the vector of ground truth fractions of sample i and $\hat{y}_i$ is the vector of predicted fractions of sample i. Each of the three ensemble models is trained independently for 5,000 steps. This 'early stopping' serves to avoid domain overfitting on the simulated tissue data, which would decrease the model performance on the real tissue RNA-seq data. We observed that training for more steps lead to an average performance decrease on real tissue RNA-seq data. To perform deconvolution with Scaden, a bulk RNA-seq sample is fed into a trained Scaden ensemble and three independent predictions for the cell type fractions of this sample are generated by the trained deep neural networks. These three predictions are then averaged per cell type to yield the final cell type composition for the input bulk RNA-seq sample:

$$\hat{y}_c = \frac{\widehat{y_c^1} + \widehat{y_c^2} + \widehat{y_c^3}}{3}$$

where $\hat{y}_c$ is the final predicted fraction for cell type c and $\widehat{y_c^i}$ is the predicted fraction for cell type c of model i.

Scaden Overview

We used several performance measures to compare Scaden to four existing cell deconvolution algorithms, CIBERSORT with LM22 GEP (CS), CIBERSORTx (CSx), MuSiC and CPM. To compare the performance of the five deconvolution algorithms we measured the root mean squared error (RMSE), Lin's concordance correlation coefficient CCC, Pearson product moment correlation coefficient r, and R^2 values comparing real and predicted cell fractions estimates. Additionally, to identify systematic prediction errors and biases, slope and intercept for the regression lines were calculated. These metrics are defined as follows:

$$RMSE(y, \hat{y}) = \sqrt{avg(y - \hat{y})^2}$$

$$r(y, \hat{y}) = \frac{cov(y, \hat{y})}{\sigma_y \sigma_{\hat{y}}}$$

$$R^2(y, \hat{y}) = r(y, \hat{y})^2$$

$$slope(y, \hat{y}) = \frac{\Delta y}{\Delta \hat{y}}$$

$$CCC(y, \hat{y}) = \frac{2r\sigma_y \sigma_{\hat{y}}}{{\sigma_y}^2 + {\sigma_{\hat{y}}}^2 + (\mu_x - \mu_{\hat{y}})}$$

where y are the ground truth fractions, $\hat{y}$ are the prediction fractions, σ_x is the standard deviation of x, $cov(y, \hat{y})$ is the covariance of y and $\hat{y}$, and $\mu_y, \mu_{\hat{y}}$ are the mean of the predicted and ground truth fractions, respectively.

All metrics were calculated for all data points of a dataset, and separately for all data points of a specific cell type. For the latter approach, we then averaged the resulting values to recover single values. While in general the metrics calculated on all data points are sufficient, good performance on cell type-level is important if one is to compare fractions of a specific cell type between samples.

CIBERSORT (CS)

CS is a cell convolution algorithm based on specialized GEPs and support vector regression. Cell composition estimations were obtained using the CS web application (https://cibersort.stanford.edu/). For all deconvolutions with CS, we used the LM22 GEP, which was generated by the CS authors from 22 leukocyte subsets profiled on the HGU133A microarray platform.

Because the LM22 GEP matrix contains cell types at a finer granularity than what was used for this study, predicted fractions of sub-cell types were added together. For cell grouping, we used the mapping of sub-cell types to broader types given by Figure 6 from Monaco *et al*.[10]. We provide a table with the exact mappings used here in the supplementary material (Table S13). The deconvolution was performed using 500 permutations with quantile normalization disabled for all datasets but GSE65133 (Microarray), as is recommended for RNA-seq data. We used default settings for all other CS parameters.

CIBERSORTx (CSx)

CSx is a recent variant of CS that can generate GEP matrices from scRNA-seq data and use these for deconvolution. For additional deconvolution robustness, it applies batch normalization to the data. All signature matrices were created by uploading the labeled scRNA-seq expression matrices and using the default options. Quantile normalization was disabled. For deconvolution on simulated data, no batch normalization was used. For all bulk RNA-seq datasets, the S-Mode batch normalization was chosen. All PBMC datasets were deconvolved using a GEP matrix generated from the data6k dataset (for simulated samples from data6k, a donorA GEP matrix was chosen).

MuSiC

MuSiC is a deconvolution algorithm that uses multi-subject scRNA-seq datasets as GEP matrices in an attempt to include heterogeneity in the matrices to improve generalization. While MuSiC tries to address similar issues of previous deconvolution algorithms by using scRNA-seq data, the approach is very different. For deconvolution, MuSiC applies a sophisticated GEP-based deconvolution algorithm that uses weighted non-negative least squares regression with an iterative estimation procedure that imposes more weight on informative genes and less weight on non-informative genes.

The MuSiC R package contains functionality to generate the necessary GEP matrix given a scRNA-seq dataset and cell type labels. To generate MuSiC deconvolution predictions on PBMC datasets, we used the data8k scRNA-seq dataset as reference data for MuSiC and follow the tutorial provided by the authors to perform the deconvolution. For deconvolution of artificial samples generated from the data8k dataset, we provided MuSiC with the data6k dataset as reference instead.

MuSiC was developed with a focus on multi-subject scRNA-seq datasets, in which the algorithm tries to take advantage from the added heterogeneity that these datasets contain, by calculating a measure of cross-subject consistency for marker genes. To assess how Scaden performs on multi-subject datasets compared to MuSiC, we evaluated both methods on artificial bulk RNA-seq samples from human pancreas {Xin et al}. We used the 'bulk_construct' function from MuSiC to combine the cells from all 18 subjects contained in the scRNA-seq dataset from Xin et al to generate artificial bulk samples for evaluation. Next, as a multi-subject reference dataset, we used the pancreas scRNA-seq dataset from Segerstolpe *et al*.[19], which contains single-cell expression data from 10 different subjects, 4 of which with type-2 Diabetes. For

Scaden, the Segerstolpe scRNA-seq dataset was split by subjects, and training datasets were generated for each subject, yielding in total 10,000 samples. For MuSiC, a processed version of this dataset was downloaded from the resources provided by the MuSiC authors[8] and used as input reference dataset for the MuSiC deconvolution. Deconvolution was then performed according to the MuSiC tutorial, and performance compared according to the above-defined metrics.

Cell Population Mapping (CPM)

CPM is a deconvolution algorithm that uses single-cell expression profiles to identify a so-called 'cell population map' from bulk RNA-seq data[9]. In CPM, the cell population map is defined as composition of cells over a cell-state space, where a cell-state is defined as a current phenotype of a single cell. Contrary to other deconvolution methods, CPM tries to estimate the abundance of all cell-states and types for a given bulk mixture, instead of only deconvolving the cell types. As input, CPM requires a scRNA-seq dataset and a low-dimensional embedding of all cells in this dataset, which represents the cell-state map. As CPM estimates abundances of both cell-states and types, it can be used for cell type deconvolution by summing up all estimated fractions for all cell-states of a given cell type - a method that is implemented in the scBio R package, which contains the CPM method. To perform deconvolution with CPM, we used the data6k PBMC scRNA-seq dataset as input reference for all PBMC samples. For samples simulated from the data6k dataset, we used the data8k dataset as reference. According to the CPM paper, a dimension reduction method can be used to obtain the cell-state space. We therefore used UMAP, a dimension reduction method widely used for scRNA-seq data, to generate the cell-state space mapping for the input scRNA-seq data. Deconvolution was then performed using the CPM function

626 of the scBio package with a scRNA-seq and accompanying UMAP embedding as
627 input.
628

List of abbreviations

RNA-seq : Next Generation RNA Sequencing

GEP : gene expression profile matrix

SVR : Support Vector Regression

DNN : Deep Neural Network

scRNA-seq : single cell RNA-seq

simulated tissue : training data generated by mixing proportions of scRNA-seq data

PBMC : peripheral blood mononuclear cells

CCC : concordance correlation coefficient

r : Pearson’s correlation coefficient

CS : CIBERSORT

CSx : CIBERSORTx

CPM : Cell Population Mapping

Author information

Affiliations

German Center for Neurodegenerative Diseases Tuebingen, Germany

Kevin Menden, Anupriya Dalmia, Peter Heutink, Stefan Bonn

Institute of Medical Systems Biology, University Medical Center Hamburg-Eppendorf, Germany

Mohamed Marouf, Stefan Bonn

Contributions

KM and SB initiated the project. KM, PH, and SB designed the study, deep learning models, and analysis. KM and MM built the deep learning models. KM, MM, and AD analyzed the data. KM and SB wrote and MM, AD, and PH contributed to the manuscript writing.

Competing interests

The authors have no competing interests.

Acknowledgements

We would like to thank the people of the Genome Biology of Neurodegenerative Diseases group and Institute of Medical Systems Biology for helpful discussions and suggestions.

Funding

This study was supported in part by RiMod-FTD a EU Joint Programme - Neurodegenerative Disease Research (JPND) to PH, KM and SFB 1286/Z2 and BMBF Integrative Data Semantics for Neurodegenerative research (IDSN) to MM.

Corresponding author

Correspondence to Stefan Bonn (sbonn@uke.de) and Kevin Menden (kevin.menden@dzne.de).

References

1. Hrdlickova, R., Toloue, M. & Tian, B. RNA-Seq methods for transcriptome analysis. *Wiley Interdiscip. Rev. RNA* **8,** (2017).

2. Egeblad, M., Nakasone, E. S. & Werb, Z. Tumors as organs: Complex tissues that interface with the entire organism. *Dev. Cell* **18,** 884–901 (2010).

3. Kuhn, A., Thu, D., Waldvogel, H. J., Faull, R. L. M. & Luthi-Carter, R. Population-specific expression analysis (PSEA) reveals molecular changes in diseased brain. *Nat. Methods* **8,** 945–947 (2011).

4. Avila Cobos, F., Vandesompele, J., Mestdagh, P. & De Preter, K. Computational deconvolution of transcriptomics data from mixed cell populations. *Bioinformatics* **34,** 1969–1979 (2018).

5. Mohammadi, S., Zuckerman, N., Goldsmith, A. & Grama, A. A Critical Survey of Deconvolution Methods for Separating Cell Types in Complex Tissues. *Proc. IEEE* **105,** 340–366 (2017).

6. Newman, A. M. *et al.* Robust enumeration of cell subsets from tissue expression profiles. *Nat. Methods* **12,** 453–457 (2015).

7. Newman, A. M. *et al.* Determining cell type abundance and expression from bulk tissues with digital cytometry. *Nat. Biotechnol.* (2019).

8. Wang, X., Park, J., Susztak, K., Zhang, N. R. & Li, M. Bulk tissue cell type deconvolution with multi-subject single-cell expression reference. *Nat. Commun.* **10,** 380 (2019).

9. Frishberg, A. *et al.* Cell composition analysis of bulk genomics using single-cell data. *Nat. Methods* **16,** (2019).

10. Monaco, G. *et al.* RNA-Seq Signatures Normalized by mRNA Abundance Allow Absolute Deconvolution of Human Immune Cell Types. *Cell Rep.* **26,**

1627–1640.e7 (2019).

11. Vallania, F. *et al.* Leveraging heterogeneity across multiple datasets increases cell-mixture deconvolution accuracy and reduces biological and technical biases. *Nat. Commun.* **9,** (2018).

12. Venet, D., Pecasse, F., Maenhaut, C. & Bersini, H. Separation of samples into their constituents using gene expression data. *Bioinformatics* **17,** 279–287 (2001).

13. Shapiro, E., Biezuner, T. & Linnarsson, S. Single-cell sequencing-based technologies will revolutionize whole-organism science. *Nat. Rev. Genet.* **14,** 618–630 (2013).

14. Schaum, N. *et al.* Single-cell transcriptomics of 20 mouse organs creates a Tabula Muris. *Nature* **562,** 367–372 (2018).

15. Kelley, K. W., Nakao-Inoue, H., Molofsky, A. V. & Oldham, M. C. Variation among intact tissue samples reveals the core transcriptional features of human CNS cell classes. *Nat. Neurosci.* **21,** 1171–1184 (2018).

16. Hicks, S. C., Townes, F. W., Teng, M. & Irizarry, R. A. Missing data and technical variability in single-cell RNA-sequencing experiments. *Biostatistics* **19,** 562–578 (2018).

17. Lin, L. I. A Concordance Correlation Coefficient to Evaluate Reproducibility *Biomatrics* **45,** 255–268 (1989).

18. Xin, Y. *et al.* RNA Sequencing of Single Human Islet Cells Reveals Type 2 Diabetes Genes. *Cell Metab.* **24,** 608–615 (2016).

19. Segerstolpe, Å. *et al.* Single-Cell Transcriptome Profiling of Human Pancreatic Islets in Health and Type 2 Diabetes. *Cell Metab.* **24,** 593–607 (2016).

20. Zimmermann, M. T. *et al.* System-wide associations between DNA-

719 methylation, gene expression, and humoral immune response to influenza
720 vaccination. *PLoS One* **11,** 1–21 (2016).
721 21. Schelker, M. *et al.* Estimation of immune cell content in tumour tissue using
722 single-cell RNA-seq data. *Nat. Commun.* **8,** 2032 (2017).
723 22. Bennett, D. A. *et al.* Religious Orders Study and Rush Memory and Aging
724 Project. *J. Alzheimer's Dis.* **64,** S161–S189 (2018).
725 23. Braak, H. & Braak, E. Neuropathological stageing of Alzheimer-related
726 changes. *Acta Neuropathol.* **82,** 239–59 (1991).
727 24. Yosinski, J., Clune, J., Nguyen, A., Fuchs, T. & Lipson, H. Understanding
728 Neural Networks Through Deep Visualization. (2015).
729 25. Athiwaratkun, B., Finzi, M., Izmailov, P. & Wilson, A. G. Improving
730 Consistency-Based Semi-Supervised Learning with Weight Averaging. *Jmlr*
731 **17,** 1–35 (2018).
732 26. Wolf, F. A., Angerer, P. & Theis, F. J. SCANPY: Large-scale single-cell gene
733 expression data analysis. *Genome Biol.* **19,** 1–5 (2018).
734 27. Satija, R., Farrell, J. A., Gennert, D., Schier, A. F. & Regev, A. Spatial
735 reconstruction of single-cell gene expression data. *Nat. Biotechnol.* **33,** 495–
736 502 (2015).
737 28. Zeisel, A. *et al.* Molecular Architecture of the Mouse Nervous System. *Cell*
738 **174,** 999–1014.e22 (2018).
739 29. Love, M. I., Soneson, C., Patro, R., Vitting-seerup, K. & Oshlack, A.
740 Swimming downstream : statistical analysis of differential transcript usage
741 following Salmon quantification. *F1000* 1–50 (2019).
742
743

Supplementary Figures & Tables

Tissue	Name	# cells	# Subjects	Source
PBMC	data6k	5,419	1	10X Genomics
PBMC	data8k	8,381	1	10X Genomics
PBMC	donorA	2,900	1	10X Genomics
PBMC	donorC	9,519	1	10X Genomics
Mouse Brain	Tasic	1,679	1	Tasic et al., Nat. Neurosci., 2016
Mouse Brain	Zeisel	3,005	1	Zeisel et al., Science, 2015
Mouse Brain	Romanov	2,881	1	Romanov et al., Nat. Neurosci., 2018
Mouse Brain	Campbell	21,086	1	Campbell et al, Nat. Neurosci., 2017
Mouse Brain	Chen	14,437	1	Chen et al., Cell Rep., 2017
Pancreas	Segerstolpe	3,514	10	Segerstolpe et al., Cell Metab., 2016
Pancreas	Baron	8,569	4	Baron et al., Cell Syst., 2016
Ascites	Ascites	3,114	3	Schelker et al, Nat. Comm., 2018

Table S1 *scRNA-seq datasets used for the generation of simulated tissues for Scaden training.*

748

Tissue	# Samples	# Datasets	Size
PBMC	32,000	4	1.2 GB
Pancreas	14,000	2	0.6 GB
Mouse Brain	30,000	5	1.5 GB
Ascites	6,000	1	0.38 GB

749 **Table S2** *Number of samples, datasets, and size of the simulated training data.*

750

751

Parameter	Values tested
Batch size	32, 64, 128, 256, 512
# Layers	2, 3, 4
Layer sizes	2048, 1024, 512, 256, 128, 64, 32, 16
Dropout rate	[0, 0.8]
Loss function	L1, L2

752 **Table S3** *Hyperparameters used for model optimization.*

753

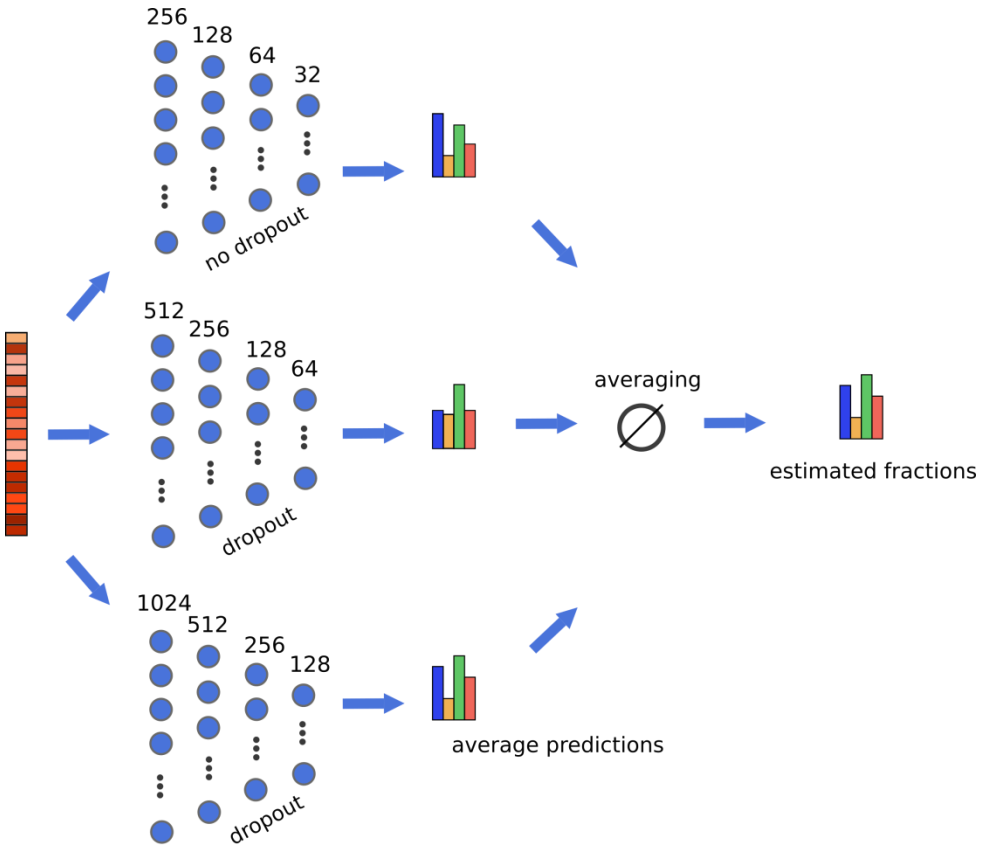

Figure S1 *Overview of the Scaden neural network ensemble model*. A bulk RNA-seq sample is the input to three separate deep neural networks with varying layer sizes and dropout regularization. The predictions of all three models are subsequently averaged to obtain the final Scaden predictions. During training, predictions are not averaged and each model is trained separately.

Model	# Layers	Layer sizes	Dropout rates
M256	4	256, 128, 64, 32	0, 0, 0, 0
M512	4	512, 256, 128, 64	0, 0.3, 0.2., 0.1
M1024	4	1024, 512, 256, 128	0, 0.6, 0.3, 0.1

761 **Table S4** *Architectures of deep neural network models used in Scaden ensemble.*

762

763

Method	DS	RMSE	Slope	Correlation	Intercept	CCC
CPM	data6k	0.189	-0.011	-0.05	0.168	-0.021
CPM	data8k	0.183	-0.002	-0.005	0.167	-0.003
CPM	donorA	0.215	-0.008	-0.046	0.168	-0.016
CPM	donorC	0.174	-0.015	-0.062	0.168	-0.026
CS	data6k	0.131	0.664	0.728	0.074	0.717
CS	data8k	0.121	0.567	0.714	0.087	0.685
CS	donorA	0.131	0.708	0.788	0.049	0.784
CS	donorC	0.131	0.742	0.719	0.079	0.688
CSx	data6k	0.1	0.83	0.854	0.05	0.844
CSx	data8k	0.134	0.601	0.662	0.082	0.651
CSx	donorA	0.045	0.9	0.979	0.017	0.975
CSx	donorC	0.11	0.819	0.811	0.07	0.776
MuSiC	data6k	0.126	0.768	0.768	0.059	0.759
MuSiC	data8k	0.135	0.597	0.659	0.083	0.648
MuSiC	donorA	0.13	0.771	0.802	0.038	0.801
MuSiC	donorC	0.132	0.815	0.737	0.07	0.704
Scaden	data6k	0.077	0.855	0.917	0.047	0.904
Scaden	data8k	0.132	0.525	0.651	0.093	0.627
Scaden	donorA	0.034	0.924	0.989	0.013	0.986
Scaden	donorC	0.109	0.848	0.821	0.067	0.786

764 **Table S5** *Deconvolution evaluation on simulated PBMC data.*

765

Method	Celltype	RMSE	Correlation	Slope	Intercept	CCC
CSx	ALPHA	0.282	0.816	0.691	0.431	0.375
CSx	BETA	0.309	0.833	0.175	-0.017	0.078
CSx	DELTA	0.04	0.812	1.567	-0.013	0.647
CSx	GAMMA	0.052	0.921	1.131	0.0	0.897
CSx	Total	0.212	0.79	1.113	-0.028	0.746
MuSiC	ALPHA	0.11	0.887	1.108	-0.042	0.863
MuSiC	BETA	0.148	0.752	1.067	0.017	0.694
MuSiC	DELTA	0.023	0.817	0.716	-0.003	0.707
MuSiC	GAMMA	0.068	0.881	0.552	-0.003	0.711
MuSiC	Total	0.099	0.938	1.078	-0.019	0.929
Scaden	ALPHA	0.067	0.949	1.071	-0.034	0.942
Scaden	BETA	0.07	0.936	1.152	-0.045	0.916
Scaden	DELTA	0.024	0.807	1.012	0.008	0.764
Scaden	GAMMA	0.045	0.914	0.89	-0.008	0.901
Scaden	Total	0.055	0.978	1.033	-0.008	0.976

Table S6 *Deconvolution performance on simulated pancreas data from Xin et al..*

770

Tissue	Name	# Samples	Reference
PBMC	PBMC1	12	Zimmermann et al., PLOS one, 2016
PBMC	PBMC2	12	Monaco et al., Cell Reports, 2019
Pancreas	Xin	18	Xin et al., Cell Metab., 2016
Human Brain	ROSMAP	390	Bennett et al., Curr Alzheimer Res., 2012
Ascites	Ascites	3	Schelker at al., Nat. Comm. 2018

771 **Table S7** *Tissue RNA-seq datasets used for performance evaluation.*

772

773

774

Method	Dataset	Celltype	RMSE	Correlation	Slope	Intercept	CCC
CPM	PBMC1	Total	0.18	-0.003	-0.003	0.167	-0.003
CPM	PBMC2	Total	0.114	-0.203	-0.094	0.182	-0.155
CS	PBMC1	Total	0.147	0.437	0.491	0.085	0.434
CS	PBMC2	Total	0.101	0.594	0.754	0.041	0.577
CSx	PBMC1	Total	0.16	0.603	0.925	0.012	0.552
CSx	PBMC2	Total	0.13	0.456	0.67	0.055	0.424
MuSiC	PBMC1	Total	0.316	-0.235	-0.468	0.245	-0.189
MuSiC	PBMC2	Total	0.299	-0.197	-0.542	0.257	-0.127
Scaden	PBMC1	Total	0.104	0.722	0.805	0.032	0.717
Scaden	PBMC2	Total	0.052	0.855	0.848	0.025	0.855

775 **Table S8** *Deconvolution performance on real PBMC RNA-seq datasets PBMC1 and*

776 *PBMC2.*

777

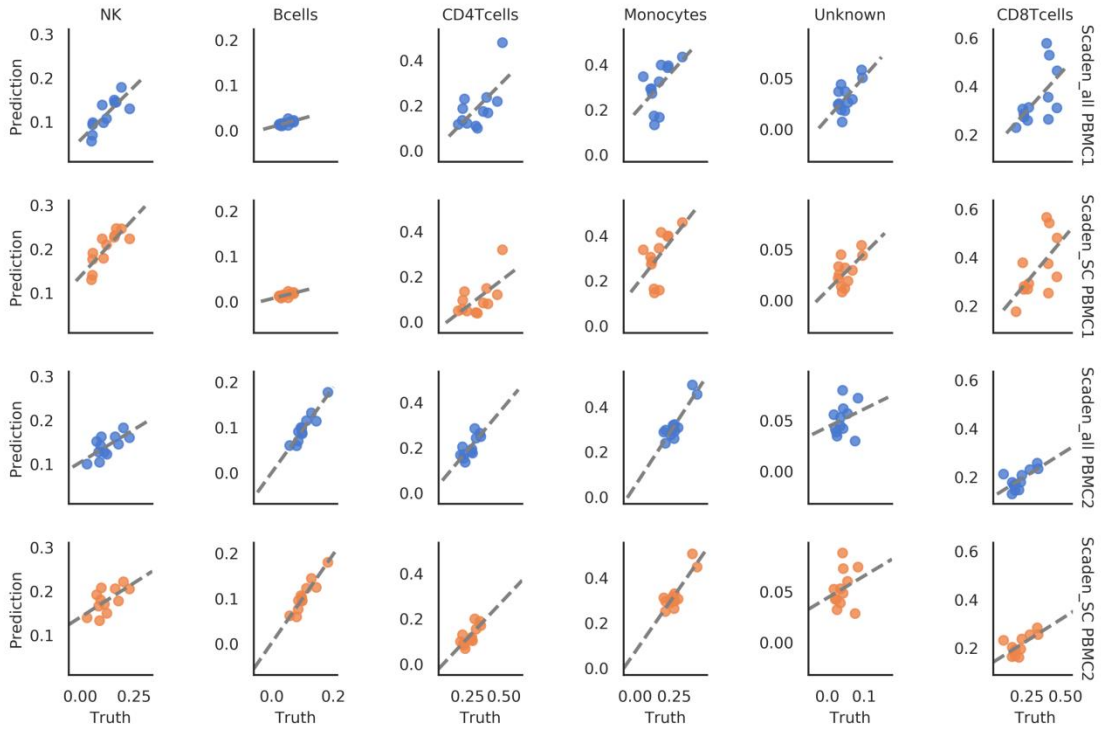

Figure S2 *Comparison of Scaden deconvolution results on PBMC1 and PBMC2 datasets with and withouth (Scaden_all, Scaden_SC, respectively) bulk RNA-seq samples included in training data*.

Method	Dataset	Celltype	RMSE	Correlation	Slope	Intercept	CCC
Scaden_SC	PBMC1	Total	0.131	0.564	0.644	0.059	0.559
Scaden_SC	PBMC2	Total	0.077	0.684	0.689	0.052	0.684
Scaden_all	PBMC1	Total	0.104	0.722	0.805	0.032	0.717
Scaden_all	PBMC2	Total	0.052	0.855	0.848	0.025	0.855
Scaden_SC	PBMC1	Bcells	0.033	0.648	0.172	0.006	0.083
Scaden_SC	PBMC1	CD4Tcells	0.228	0.633	0.492	-0.055	0.149
Scaden_SC	PBMC1	CD8Tcells	0.101	0.603	0.761	0.108	0.562
Scaden_SC	PBMC1	Monocytes	0.178	0.556	0.885	0.173	0.186
Scaden_SC	PBMC1	NK	0.087	0.81	0.531	0.137	0.312
Scaden_SC	PBMC1	Unknown	0.029	0.577	0.361	0.009	0.287
Scaden_SC	PBMC2	Bcells	0.012	0.936	0.977	0.002	0.935
Scaden_SC	PBMC2	CD4Tcells	0.145	0.767	0.682	-0.057	0.119
Scaden_SC	PBMC2	CD8Tcells	0.049	0.67	0.403	0.129	0.587
Scaden_SC	PBMC2	Monocytes	0.078	0.865	0.994	0.071	0.558
Scaden_SC	PBMC2	NK	0.071	0.629	0.314	0.14	0.276
Scaden_SC	PBMC2	Unknown	0.025	0.247	0.217	0.044	0.209
Scaden_all	PBMC1	Bcells	0.031	0.668	0.188	0.007	0.1
Scaden_all	PBMC1	CD4Tcells	0.151	0.638	0.652	-0.017	0.345
Scaden_all	PBMC1	CD8Tcells	0.096	0.6	0.704	0.123	0.569
Scaden_all	PBMC1	Monocytes	0.172	0.518	0.777	0.184	0.177
Scaden_all	PBMC1	NK	0.036	0.804	0.488	0.058	0.71
Scaden_all	PBMC1	Unknown	0.026	0.64	0.41	0.01	0.365
Scaden_all	PBMC2	Bcells	0.013	0.936	0.94	0.0	0.917
Scaden_all	PBMC2	CD4Tcells	0.074	0.772	0.769	-0.005	0.373
Scaden_all	PBMC2	CD8Tcells	0.051	0.672	0.398	0.106	0.562
Scaden_all	PBMC2	Monocytes	0.072	0.895	1.058	0.049	0.614
Scaden_all	PBMC2	NK	0.045	0.69	0.301	0.103	0.467
Scaden_all	PBMC2	Unknown	0.023	0.241	0.178	0.043	0.203

Table S9 *Deconvolution performance on real PBMC RNA-seq data for Scaden models trained only on scRNA-seq simulated tissues (Scaden_SC) or on a mix of simulated and real tissue data (Scaden_all).*

Method	Type	CCC	Correlation	Intercept	RMSE	Slope
CPM	Total	-0.0	0.004	0.153	0.183	-0.0
CSx	Total	0.938	0.952	0.002	0.069	1.115
MuSiC	Total	0.876	0.907	0.033	0.079	0.696
Scaden	Total	0.948	0.955	-0.030	0.061	1.066

788 **Table S10** *Deconvolution performance on real Ascites RNA-seq data.*

789

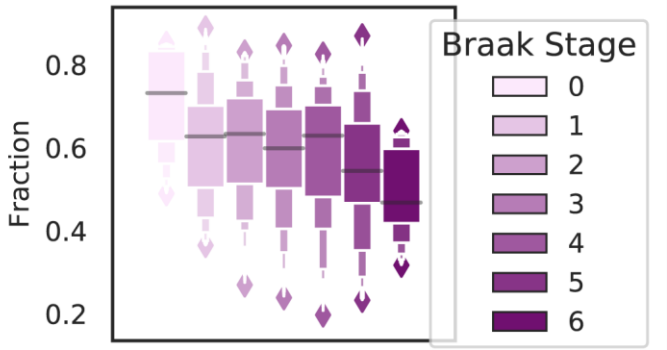

Figure S3 *Deconvolution performance on real human brain RNA-seq data.* Scaden was trained on mouse scRNA-seq data and the trained model was used to deconvolve cell fractions of ROSMAP human brain RNA-seq data. This data does not contain cell fraction ground-truth information. Instead, the box plot shows the decrease of neuronal cell fractions with increasing Braak disease stage, a well-known phenomenon in AD.

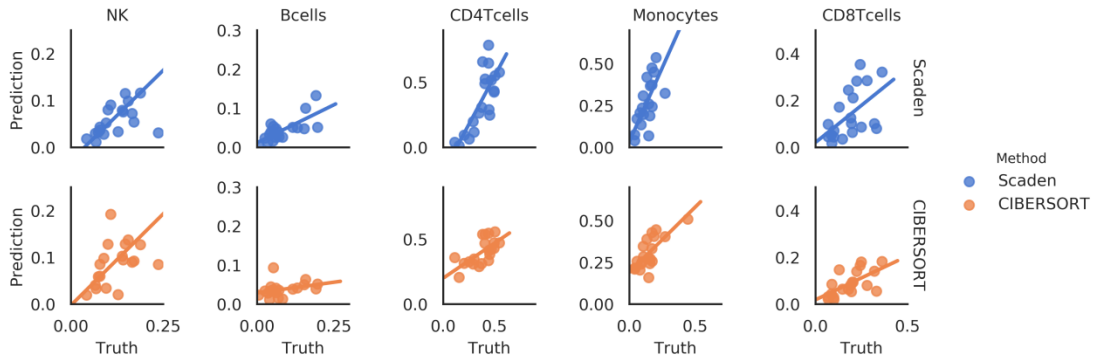

Figure S4 *Deconvolution performance comparison of CS (LM22) and Scaden on the GSE65133 PBMC microarray dataset*.

801

Method	Celltype	CCC	Correlation	Intercept	RMSE	Slope
CS	Bcells	0.122	0.33	0.029	0.068	0.109
CS	CD4Tcells	0.629	0.658	0.199	0.095	0.537
CS	CD8Tcells	0.285	0.635	0.018	0.12	0.375
CS	Monocytes	0.295	0.741	0.19	0.17	0.779
CS	NK	0.623	0.698	-0.003	0.059	0.78
CS	Total	0.717	0.728	0.026	0.11	0.869
Scaden	Bcells	0.431	0.728	0.012	0.055	0.388
Scaden	CD4Tcells	0.64	0.778	-0.195	0.153	1.474
Scaden	CD8Tcells	0.474	0.543	0.02	0.104	0.635
Scaden	Monocytes	0.43	0.838	0.033	0.191	1.764
Scaden	NK	0.516	0.741	-0.029	0.074	0.77
Scaden	Total	0.705	0.749	-0.015	0.126	1.067

802 **Table S11** *Deconvolution performance on real PBMC microarray data.*

803

804

Software	Version
pandas	0.23.4
Python	3.6.8
Tensorflow	1.10.0
matplotlib	2.2.3
nb_conda	2.2.1
numpy	1.15.0
scipy	1.1.0
seaborn	0.9.0
anndata	0.6.9
scanpy	1.2.2
scikit-learn	0.20.0
ipython	6.5.0
python-igraph	0.7.1.post6
louvain	0.6.1
tqdm	4.7.2
igraph	0.7.1

805 **Table S12** *Software packages and versions used.*

806

807

Target Cell Type	LM22 Cell Types
B cells	B cells naive, B cells memory
CD8 T cells	T cells CD8, T cells follicular helper, T cells gamma delta
CD4 T cells	T cells CD4 naive, T cells regulatory (Tregs), T cells CD4 memory resting, T cells CD4 memory activated
NK	NK cells resting, NK cells activated
Dendritic	Dendritic cells resting, Dendritic cells activated
Monocytes	Monocytes, Macrophages M0, Macrophages M1, Macrophages M2
Unknown	Mast cells resting, Mast cells activated, Eosinophils, T cells folicular helper, T cells gamma delta, Plasma cells, Neutrophils, Dendritic

808 **Table S13** *Mapping of the LM22 GEP to cell types.*

809